International Journal of Mass Spectrometry 446 (2019) 116233

Contents lists available at ScienceDirect

International Journal of Mass Spectrometry

journal homepage: www.elsevier.com/locate/ijms

Calibration of parent and fragment ion detection rates in Rosettas ROSINA/DFMS mass spectrometer

J. De Keyser [a, b, *], A. Gibbons [a, c], F. Dhooghe [a], K. Altwegg [a], H. Balsiger [d], J.-J. Berthelier [e], S.A. Fuselier [f, g], T.I. Gombosi [h], E. Neefs [i], M. Rubin [d]

[a] Space Physics Division, Royal Belgian Institute for Space Aeronomy, Ringlaan 3, B-1180, Brussels, Belgium
[b] Center for Plasma Astrophysics, Katholieke Universiteit Leuven, Celestijnenlaan 200B, B-3001, Heverlee, Belgium
[c] Quantum Chemistry and Photophysics Laboratory, Université Libre de Bruxelles, Av. F. D. Roosevelt 50, B-1050, Brussels, Belgium
[d] Physikalisches Institut, University of Bern, Sidlerstr. 5, CH-3012, Bern, Switzerland
[e] LATMOS/IPSL-CNRS-UPMC-UVSQ, 4 Av. de Neptune, F-94100, Saint-Maur, France
[f] Space Science Directorate, Southwest Research Institute, 6220 Culebra Road, San Antonio, TX, 78228, USA
[g] Department of Physics and Astronomy, University of Texas at San Antonio, San Antonio, TX, 78249, USA
[h] Department of Atmospheric, Oceanic and Space Sciences, University of Michigan, 2455 Hayward, Ann Arbor, MI, 48109, USA
[i] Engineering Division, Royal Belgian Institute for Space Aeronomy, Ringlaan 3, B-1180, Brussels, Belgium

ARTICLE INFO

Article history:
Received 19 April 2019
Received in revised form
18 September 2019
Accepted 29 September 2019
Available online 3 October 2019

Keywords:
Mass spectrometry
Data calibration
Secondary electron yield
Comet atmosphere
Rosetta

ABSTRACT

The Double Focusing Mass Spectrometer DFMS embarked on the European Space Agency's Rosetta mission as part of the ROSINA instrument suite. It boasts a high mass resolution and a high sensitivity, which have guaranteed spectacular discoveries during Rosetta's rendez-vous with comet 67P/Churyumov-Gerasimenko. This paper describes the DFMS data calibration procedure for determining the parent and fragment ion count rates in the neutral mode, which serve as the basis for retrieving the neutral gas densities. A new approach to computing secondary electron yields is presented. Attention is given to an analysis of the mass peak shapes, which change with magnet temperature. Discrete counting statistical effects also affect the peak shape at low counts. If not accounted for, changes of mass peak shape can induce errors of up to 20% on the determination of the ion fluxes. An assessment of the different sources of uncertainty on the obtained count rates and ratios of count rates is presented.

© 2019 The Authors. Published by Elsevier B.V. This is an open access article under the CC BY-NC-ND license (http://creativecommons.org/licenses/by-nc-nd/4.0/).

1. Introduction

DFMS is the Double Focusing Mass Spectrometer, part of the ROSINA instrument [1] onboard the Rosetta spacecraft of the European Space Agency, that has made a number of discoveries during Rosetta's rendezvous with comet 67P/Churyumov-Gerasimenko [e.g. Refs. [2–6]]. The instrument was designed to measure neutral atoms and molecules as well as naturally occurring ions, providing both the high sensitivity and high mass resolution ($m/\Delta m = 3000$ at the 1% level in high resolution mode) that were essential for the detection of minor constituents in the cometary atmosphere and for determining isotopic composition. This was achieved by acquiring detailed mass spectra over successive mass intervals that scan the range 13–150 Da/ e.

The operation of the DFMS spectrometer has been explained at length in Ref. [1]. This paper addresses the neutral mode, in which incoming neutral atoms or molecules enter the instrument source where a fraction of them are ionized accompanied by some fragmentation into neutral and ionized fragments. The impacting electrons are emitted by a filament and accelerated to an energy of 45 eV (lower than the typical 70 eV in order to enhance the production of parent ions and to reduce fragmentation). The resulting parent and fragment ions are extracted from the source and accelerated, and pass through an electrostatic and a magnetic sector. The ion optics include a zoom system to enhance the dispersion, which results in an increased mass resolution as the spatial resolution of the detector is fixed; only the high resolution case is discussed here. DFMS's principal detector is a combination of a micro-channel plate (MCP) and a linear CCD chip (the Linear Electron Detector Array or LEDA). The MCP consists of two parallel plates with 6 μm diameter pore channels in chevron configuration, at a 15° angle with the plate surface [7]. The LEDA features two

* Corresponding author. Space Physics Division, Royal Belgian Institute for Space Aeronomy, Ringlaan 3, B-1180, Brussels, Belgium.
E-mail address: Johan.DeKeyser@aeronomie.be (J. De Keyser).

https://doi.org/10.1016/j.ijms.2019.116233
1387-3806/© 2019 The Authors. Published by Elsevier B.V. This is an open access article under the CC BY-NC-ND license (http://creativecommons.org/licenses/by-nc-nd/4.0/).

parallel rows with 512 charge collecting anodes each, with separate read-out electronics for redundancy reasons [8]. The ions hit the MCP and produce a cascade of electrons as a potential difference is applied across the MCP, thus setting the gain as it determines by how much the incoming ion current is multiplied upon conversion into an electron current. The electrons that exit the MCP are registered by the LEDA anodes or pixels. The charge collected by the anodes is digitized by an analog-to-digital converter (ADC) providing the counts per pixel, which are transmitted to Earth together with instrument housekeeping information. This results in raw spectra that exhibit peaks corresponding to the various ions (Fig. 1).

The interpretation of DFMS mass spectra proceeds in several steps. First, there is the calibration of the mass scale, i.e., assigning masses to the pixels. Then, the ADC counts must be translated into corresponding ion count rates for each of the mass peaks. This involves peak fitting of the spectra to identify the contributions of the various fragments from higher mass molecules. Knowing the fragmentation patterns and the instrument sensitivities, one can then in principle obtain the ambient neutral gas densities. In practice, the values obtained are rescaled so as to match the total gas density as measured by the ROSINA COPS sensor [1,9].

Each step in the calibration procedure is characterized by uncertainties. The error on the final result is the accumulation of the errors in each step. The objective of the present study is to determine the ion count rates as accurately as possible. Section 2 explains the basic data analysis procedure. A first part of the study proposes a consistent approach for determining the secondary electron yields involved in the MCP gain (section 3). A second part addresses changes of the mass peak shape (section 4) and describes how these are dealt with (section 5). The paper concludes with a summary and a discussion of the uncertainties on the ion count rates.

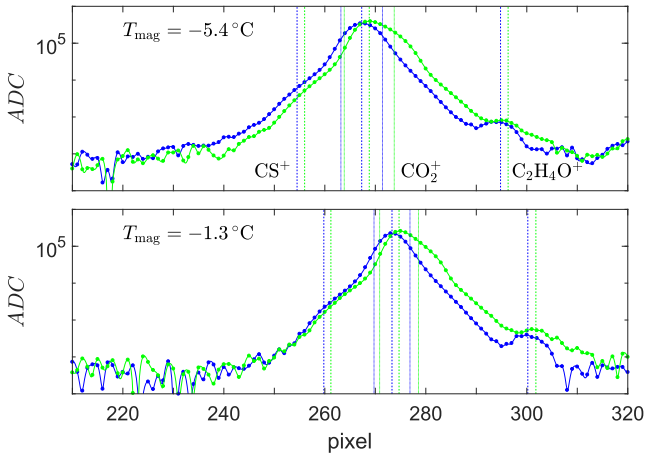

Fig. 1. Raw DFMS spectra of the CO_2^+ peak obtained (a) on 2014-10-02 00:11:39–00:11:59 when the magnet temperature was $T_{mag} = -5.4\,^{\circ}C$, and (b) on 2014-10-02 23:19:41–23:20:01 when $T_{mag} = -1.3\,^{\circ}C$, after subtraction of the detector offset, for LEDA channel A (blue) and B (green). After accounting for the position-dependent gain, a peak fit procedure has been performed with a common peak shape for all contributing constituents (CO_2^+ main peak, CS^+ bump on the left flank of the main peak, smaller $C_2H_4O^+$ peak to the right). The fitted peak positions are indicated with dashed lines. The fitted peak widths (1 σ intervals) are indicated for CO_2^+ with dotted lines (but are identical for the other ions). Position and width change with magnet temperature; in the low temperature case the peaks are about 15% wider for channel A and about 20% for channel B. Both spectra were taken in the same instrument mode (at gain step 15 and 14, respectively, but gain step has no impact on peak width). (For interpretation of the references to colour in this figure legend, the reader is referred to the Web version of this article.)

2. Calibration procedure

DFMS measures a spectrum over a limited mass range around a commanded mass-over-charge value m_0; note that most of the parent and fragment ions are singly charged so that $m/Z = m$. In high resolution mode, the width of the mass range on the LEDA detector is about $0.016\,m_0$. One pixel corresponds to $\Delta m_{pixel} = 3.4 \times 10^{-5}\,m_0$. At the mass of CO_2^+, a pixel is 0.0015 Da wide. Mass peaks have a full width at half maximum of ~ 9 pixels resulting in a mass resolution $m/\Delta m_{FWHM} = 4000$. If the mass peak shape is known, adjacent peaks of similar intensity only a few pixels apart may still be separated.

2.1. Mass calibration

The standard mass calibration formula used for translating pixel number p into the corresponding mass m is

$$m(p) = m_0 e^{(p-p_0)\frac{x}{ZF\,d}} \quad (1)$$

where $p_0 = 256.5$ is the pixel position at the middle of the detector, $x = 25\ \mu$m is the separation between the centres of successive pixels, $d = 127000\ \mu$m is the mass dispersion factor, and $ZF = 6.4$ is the zoom factor for the high resolution mode. Instrumental effects lead to noticeable deviations from this formula. An improved mass calibration can be obtained by collecting peak identifications (triplets (m_{0k}, m_k, p_k)) for many spectra over a whole range of commanded mass-over-charge values to produce fits of the form $p_0 = 256.5 + \Delta p_0(m_0)$ and $ZF = ZF(m_0)$. A further improvement is achieved by determining the pixel shift as $p_0 = 256.5 + \Delta p_0(m_0) + \Delta p_0(t)$, where the time-dependent term captures how the peak shift varies with the temperature of the instrument optics (characterized by the magnet temperature T_{mag}). This term is obtained by noting how the pixel position of the well identified CO_2^+ peak varies with time. An example of such a temperature-dependent shift is visible in Fig. 1. The mass calibration relation also takes care of a change in instrument settings in early 2016 to guide the beam onto a less used part of the detector.

2.2. MCP gain

The calibration of the signal intensity must account for the conversion of the incoming ion flux by the MCP-LEDA combination into a (much larger) electron flux on the detector, which is the so-called gain, and for the conversion of the collected electrons into a digital representation.

The gain is essentially a property of the MCP and depends on the gain potential across the MCP, on the position along the mass analysis direction, and on time. The gain has been experimentally determined before launch [10]. DFMS has 16 gain steps, each step amplifying the signal by a factor ~ 2.6, corresponding to increasing voltage differences across the MCP (about 50 V per step). A built-in automatic gain control algorithm [11] adapts the gain step to ensure a strong signal while operating the detector in its linear regime and avoiding saturation [12]. The position- and time-dependence stems from detector ageing. In most (high resolution) mass spectra the peaks are situated between pixels 200 and 310. The inner surface of the MCP pores in the centre of the detector therefore degrades more rapidly as a consequence of the repeated ion bombardment, mostly through sputtering and ion implantation [13], so that the gain decreases [14]; this is why the instrument settings were changed in early 2016 to shift the average peak position by ~ 60 pixels. The position dependence has been verified in flight repeatedly by scanning the H_2O^+ peak across the MCP/LEDA detector to determine the relative pixel responses, for various gain

steps [see Ref. [15], supplementary material]. The evolution of the gain factors can be assessed in flight by comparing count rates for a given ion obtained with different gain steps. Finally, as an absolute reference, one can use the total gas density provided by the COPS sensor [1,9].

For convenience, the gain is split up into two factors:

$$G(p,g,t) = G_{\mathrm{ov}}(g,t)\; G_{\mathrm{pgc}}(p,g,t), \tag{2}$$

where g is the gain step, t is time and p position, and with the normalization $\max_p G_{\mathrm{pgc}}(p,g,t) = 1$. The gain variation across a single spectrum is concentrated in the position-dependent gain correction factor $G_{\mathrm{pgc}}(p,g,t)$, while $G_{\mathrm{ov}}(g,t)$ captures the overall gain level. A technique for correcting for the position-dependent gain has been recently proposed in Ref. [16]. If $\psi(p,p')$ is the electron response on the LEDA at pixel p when an ion impinges at MCP position p', and if $\mathbf{G}_{\mathrm{pgc}}(g,t) = \mathrm{diag}\; G_{\mathrm{pgc}}(p_i,g,t)$ is a diagonal matrix representing the position-dependent gain, a LEDA signal $F(p_i)$ can be corrected for position-dependent gain degradation by $\tilde{\mathbf{F}} = \mathbf{T}^{-1}(\mathbf{I})\,\mathbf{T}(\mathbf{G}_{\mathrm{pgc}})\,\mathbf{F}$, with the transformation matrix $\mathbf{T}(\mathbf{D})$ defined by $T_{sj} = D_{jj}\,\psi_{sj}$, $\mathbf{D}$ being a diagonal matrix. The recorded ADC counts are thus first corrected by

$$\widetilde{\mathbf{ADC}} = \mathbf{T}^{-1}(\mathbf{I})\;\mathbf{T}(\mathbf{G}_{\mathrm{pgc}})\;\left[\mathbf{ADC} - \mathbf{ADC}_{\mathrm{offset}}\right] \tag{3}$$

where $\mathbf{ADC}$ represents the LEDA counts and $\mathbf{ADC}_{\mathrm{offset}}$ the offset due to thermal and read-out noise in the LEDA [10]. The corrected values are converted into ion count rate spectra using

$$\widehat{R}(p) = \frac{U_{\mathrm{ADC}}\; C_{\mathrm{LEDA}}}{e\;\Delta t\; G_{\mathrm{ov}}(g,t)}\,\widetilde{ADC}(p) \tag{4}$$

where $C_{\mathrm{LEDA}} = 4.22 \times 10^{-12}$ F is the capacitance of a LEDA pixel, $U_{\mathrm{ADC}} = 6.105 \times 10^{-4}$ V is the ADC conversion factor, and $\Delta t =$ 19.66 s is the total integration time (an accumulation of 3000 individual 6.554 ms spectra). Note that G and G_{ov} are associated with incident ions of a given reference species at its reference energy $\mathscr{E}^*$. The reference species is N_2^+ at an energy of 3050 eV [10].

There are different options (identified below with a superscript) for computing the ion count rate spectrum $\widehat{R}(p)$, depending on how the gain $G_{\mathrm{ov}}(g,t)$ is defined.

Option 1 With $\widetilde{ADC}^*(g,t)$ the average peak height recorded at time t for gain step g (after position-dependent gain correction) when a single reference ion arrives on the MCP with energy $\mathscr{E}^*$, the standard definition of the gain is

$$G_{\mathrm{ov}}^{(1)}(g,t) = \frac{U_{\mathrm{ADC}}\; C_{\mathrm{LEDA}}}{e}\,\widetilde{ADC}^*(g,t), \tag{5}$$

so that $G_{\mathrm{ov}}^{(1)}(g,t)$ is expressed as ADC counts per ion. The MCP peak height generated by an ion has a certain pulse height distribution, due to the stochastic nature of the secondary electron production process, particularly in the first stages of the cascade [14,17,18]. Hence, $G_{\mathrm{ov}}^{(1)}(g,t)$ refers to the modal gain. Plugging $G_{\mathrm{ov}} = G_{\mathrm{ov}}^{(1)}$ into Eq. (4) gives $\widehat{R}^{(1)}(p)$ in ions·s^{-1}. With this definition of the gain, the quantity that characterizes a mass peak at pixel p^* is its height. For reference ions reaching the MCP with energy $\mathscr{E}^*$, the count rate is $R = \widehat{R}^{(1)}(p^*)$, which can be immediately read off a spectrum by looking at the height of the mass peak (at least approximately).

Option 2 Alternatively, one can characterize a mass peak by its peak area

$$IR = \int_{-\infty}^{+\infty} \widehat{R}^{(2)}(p)\,\mathrm{d}p. \tag{6}$$

This definition is more natural if one considers $\widehat{R}^{(2)}(p)$ to be a spectrum over the pixels, expressed in ions·s^{-1}·pixel^{-1}. If $\psi(p,p')$ is the peak shape function for a peak at position p', normalized so that its maximum is 1, then ideally $\widehat{R}^{(2)}(p) = R\,\psi(p)$ if this is the only peak. This corresponds to a gain factor $G_{\mathrm{ov}}^{(2)}(g,t) = G_{\mathrm{ov}}^{(1)}(g,t)\Psi$, with

$$\Psi = \int_{-\infty}^{+\infty} \psi(p,p')\;\mathrm{d}p, \tag{7}$$

expressed in pixels. As a result, $\widehat{R}^{(2)}(p) = \widehat{R}^{(1)}(p)/\Psi$.

Option 3 A slight variant is to characterize a mass peak by

$$R = \int_{-\infty}^{+\infty} \widehat{R}^{(3)}(m)\mathrm{d}m. \tag{8}$$

This definition fits the concept that $\widehat{R}^{(3)}(m)$ is a mass spectrum, in ions·s^{-1}·Da^{-1}. The gain factor then is $G_{\mathrm{ov}}^{(3)}(g,t) = G_{\mathrm{ov}}^{(1)}(g,t)\;\Psi\;\Delta m_{\mathrm{pixel}}$ and is expressed in Da. One finds that $\widehat{R}^{(3)}(p) = \widehat{R}^{(2)}(p)/\Delta m_p = \widehat{R}^{(1)}(p)/\Psi\;\Delta m_{\mathrm{pixel}}$.

Options 2 and 3 are essentially identical. They correspond to the first option only if the peak shape ψ, and hence Ψ, always remains the same.

Peak fitting of the mass spectra provides the value of R_k for each ion k in the spectrum. Since the MCP gain is defined relative to the 3050 eV N_2^+ reference ions, the true ion count rates $\mathscr{R}_k$ must take into account the relative secondary electron yields μ_k for the impact of the ions on the MCP at their actual energy attained in DFMS, compared to the reference species and energy, so that

$$\mathscr{R}_k = \frac{R_k}{\mu_k}. \tag{9}$$

The computation of the secondary electron yields is addressed in section 3.

Detector ageing leads to a decrease in the total gain. It manifests itself both as a reduction of the secondary electron yield of an impacting ion and as a reduction of the electron amplification within the MCP pores. Since there are no measurements available to distinguish between both, ageing is modelled here solely through a position-dependent reduction of the gain, while keeping the yields constant [16].

2.3. From ion count rates to abundances

Converting ion count rates into abundances of neutral atoms and molecules requires an additional step [19]. The number of atoms or molecules of species j that produce ion k is proportional to their ambient density n_j and to the filament emission current $I_{\mathrm{em},k}$ in the source while the ion is measured; the proportionality factor is the sensitivity S_j for the given species, which depends on the electron impact ionization cross section. The fragmentation fractions F_{jk} (with $\sum_k F_{jk} = 1$) give the relative amounts of the fragmentation products of species j as created in the ion source. The DFMS high mass resolution measurements at the comet always used the same (maximum) emission current (200 μA) and the fragmentation pattern can be considered constant. The fraction of ions that reach the MCP depends on the efficiency of ion extraction from the source and transport through the optics, described by the

transmission coefficient τ, which is a smooth function of m/Z and does not depend on the chemical identity of the ion. One must disentangle the contributions from the different neutral species to the ion detection rates by solving the system

$$\mathscr{R}_k = \sum_j n_j\, I_{\mathrm{em},k}\, S_j\, F_{jk}\, \tau_k, \tag{10}$$

or, equivalently,

$$R_k = \sum_j n_j\, I_{\mathrm{em},k}\, S_j\, F_{jk}\, \tau_k\, \mu_k. \tag{11}$$

There is an equation for each parent−ion pair. One has to make sure that the system is overdetermined. One does not know a priori which neutral parents exist, but plausible candidates can be identified from comet and interstellar cloud composition studies and include isotopologues thereof. Also, the fragmentation patterns and sensitivities are not well known for many species. Nevertheless, interesting results have been obtained in a fair number of situations. A case in point is given in Ref. [20].

The above equations are often simplified for practical reasons. If no information is available regarding the transmission coefficients, one can absorb these into the sensitivity and the fragmentation fractions, leading to

$$S'_j = S_j \sum_k F_{jk}\, \tau_k, \tag{12}$$

$$F'_{jk} = \frac{F_{jk}\, \tau_k}{\sum_k F_{jk}\, \tau_k}, \tag{13}$$

$$R_k = \sum_j n_j\, I_{\mathrm{em},k}\, S'_j\, F'_{jk}\, \mu_k, \tag{14}$$

where the F'_{jk} still define a fragmentation pattern since $\sum_k F'_{jk} = 1$. An alternative is to also include the secondary electron yields into the sensitivity and the fragmentation fractions according to

$$S''_j = S_j \sum_k F_{jk}\, \tau_k\, \mu_k, \tag{15}$$

$$F''_{jk} = \frac{F_{jk}\, \tau_k\, \mu_k}{\sum_k F_{jk}\, \tau_k\, \mu_k}, \tag{16}$$

$$R_k = \sum_j n_j\, I_{\mathrm{em},k}\, S''_j\, F''_{jk}, \tag{17}$$

where the F''_{jk} define a fragmentation pattern since $\sum_k F''_{jk} = 1$. Equations (11), (14) and (17) are equivalent. Variants can be derived when not all electron impact ionization products can be measured (implying a renormalization of the fragmentation fractions and a corresponding change in sensitivity) or when fragmentation fractions are normalized differently (e.g., relative to the dominant ion). Equation (17) allows to derive the S''_j and F''_{jk} when simultaneous n_j and R_k data are available as during laboratory calibration activities [21]. The fragmentation patterns F_{jk}, F'_{jk}, and F''_{jk} all represent something different, so one must not mix them up. Extreme care has to be taken when using fragmentation patterns from NIST [22] or elsewhere for the interpretation of DFMS data, also because the DFMS electron impact ionization source operates at 45 eV while the NIST data mostly correspond to 70 eV. Note that the sensitivities depend on the choice of reference species and energy in the definition of the gain.

3. Secondary electron yield

The secondary electron yield γ_k describes the ability of an impacting ion to produce secondary electrons on the inner surface of the MCP pores. Secondary electron production stems at low energies from potential electron emission due to the transfer of potential energy to an electron upon neutralisation of the incident ion, and at higher energies from kinetic electron emission processes that involve interactions between the electrons of the incident ion and of the target material [23–25].

3.1. Basic description

Ions hit the inner walls of the MCP pores at shallow incidence and with a significant speed. Also, most ions are singly charged, so that their internal potential is limited. This implies that the role of potential electron emission is relatively limited [26]. Kinetic electron emission is promoted at shallow incidence as the incoming ion spends more time just below the impacted surface and has ample occasion to excite electrons in the solid [27,28]. For grazing incidence and high ion speed, binary scattering of the ions with the surface valence electrons is the dominant process, leading to electron ejection peaked in the direction of reflection [28].

The probability of escape for a quasi-free electron depends on the Fermi energy and on the work function of the solid; these values set a rather sharp threshold on the minimum energy (or, equivalently, velocity) the incident ion should have to produce escaping electrons. The assumption of quasi-free electron collisional excitations, however, is not valid at low impact speed. It has been shown that the partial localization of quasi-free electrons due to the presence of the surface softens the transition; in addition, low ion speeds may lead to multiple-electron excitations which also lead to sub-threshold electron emission [29,30]. Often some potential emission cannot be excluded either.

The secondary electron yield of an atomic ion bombarding a substrate can be approximated (at least in the high-velocity case) by

$$\gamma_k = a_k\, v \arctan[b_k(v - v_{\mathrm{lim}})], \tag{18}$$

where $v = \sqrt{2\mathscr{E}/m_k}$ is the ion velocity, v_{lim} is the aforementioned velocity threshold (typically $\sim 10^4\ \mathrm{m{\cdot}s^{-1}}$), and a_k and b_k are empirical constants that characterize the interaction of the ion and the target material [24,31]. For velocities $v \gg v_{\mathrm{lim}}$, Eq. (18) simplifies to

$$\gamma_k \approx \frac{\pi}{2}\, a_k\, v - \frac{a_k}{b_k} \approx \frac{\pi}{2}\, a_k\, v, \tag{19}$$

where v_{lim} plays no role anymore. For very large ion velocities, only a_k matters. For ion velocities slightly above v_{lim} one has

$$\gamma_k \approx a_k\, b_k\, v\, (v - v_{\mathrm{lim}}). \tag{20}$$

One can compute the secondary electron yield for molecular ions by adding the contributions for atomic ions in the form

$$\gamma_k = \sum_i n_i\, \gamma_i, \tag{21}$$

where the sum is over all constituent atoms [24,31].

3.2. Secondary electron yields for DFMS

The number of electrons produced in the MCP per incident ion is $\mu_k G$, with $\mu_k = \gamma_k/\gamma^*$ the relative secondary electron yield and with

γ^* the (absolute) yield of 3050 eV N_2^+ ions. While absolute yields are limited by the MCP aperture ratio [32,33], this factor is eliminated by considering relative yields.

The energy of an ion hitting the MCP is $\mathscr{E} = Z_k e(V_{\text{accel}} + V_{\text{post-accel}})$, where V_{accel} is the acceleration voltage needed to pass through the electrostatic and magnetic sectors, and $V_{\text{post-accel}}$ is a post-acceleration voltage that is applied to ensure that the ion hits the MCP with sufficient energy so as to produce enough electrons. The acceleration potential required by the ion optics depends on the commanded mass m_{0k} at which fragment ion k is detected through

$$V_{\text{accel}} = \frac{e\, r_{\text{magnet}}^2\, B^2}{2 m_{0k}}. \tag{22}$$

In the absence of post-acceleration, assuming the DFMS magnet to have a constant given strength, taking $m_{0k} \approx m_k$, and relying on Eq. (19), the relative yield can be found as

$$\mu_k = \sqrt{\frac{Z_k}{Z^*}}\, \frac{a_k}{a^*}\, \frac{m^*}{m_k}, \tag{23}$$

where Z^*, m^* and a^* represent the charge, mass, and yield coefficient of the reference ion, respectively. For singly charged ions ($Z_k = Z^* = 1$) and ignoring the chemical identity of the atomic building blocks ($a_k = a^*$), one finds

$$\mu_k \approx \widehat{\mu}_k = \frac{m^*}{m_k}. \tag{24}$$

Relying on Eq. (20) for smaller velocities, one has

$$\mu_k \approx \tilde{\mu}_k = \frac{m^*}{m_k}\left(\frac{m^*}{m_k} - \frac{m^*}{m_{\text{lim}}}\right) \tag{25}$$

with $m_{\text{lim}} = e\, r_{\text{magnet}}\, B / v_{\text{lim}}$ being larger than the m_k but not by very much. Each approximation going into Eqs. (24) and (25) is discussed below.

Most ions have masses m_k less than 0.2 % from their respective integer commanded mass-over-charge m_{0k}.

The strength of the DFMS magnet depends on its temperature. A feedback loop adapts V_{accel} to compensate for this dependence based on real-time measurement of T_{mag}. The field strength for the flight instrument's magnet [34] is

$$B(T_{\text{mag}}) = 0.3550 - 1.7262 \times 10^{-4}\ (T_{\text{mag}} - T_0)\ \ [\text{T}], \tag{26}$$

where $T_0 = -22\,^\circ$C. In operation near the comet, T_{mag} varied between $-10\,^\circ$C and $+5\,^\circ$C, implying a change of 0.7 % in magnetic field strength and ion speed. The potentials in DFMS can be set only with a finite precision so that the applied acceleration differs slightly from the desired one by up to ~ 0.2 %, leading to a 0.1 % uncertainty on v_k. The actual potentials are measured and reported in the instrument housekeeping with 0.1 % precision, so this can be properly accounted for.

For low masses a small post-acceleration $V_{\text{post-accel}} = 50$ V is always applied. The error on the ion energy due to ignoring this post-acceleration voltage ranges from 1 % at $m_0 = 13$ Da up to 5 % at $m_0 = 69$ Da; the error on the ion speed ranges from 0.5 % to 3 %. For $m_0 \geq 70$ Da, DFMS employs a post-acceleration of 981 V. The high-mass case is not considered here further since the strong post-acceleration electric field is non-uniform, which adds another degree of complexity to the analysis.

Giotto's NMS and Rosetta's DFMS spectrometers had MCPs made of similar material, but both worked with different acceleration potentials. It is therefore not justified to use the secondary electron yields established for NMS to interpret DFMS measurements. However, one can use the coefficients reported for the NMS MCP [[31], Table 2] in combination with the acceleration characteristics of DFMS to compute the relative yields μ_k for DFMS. These values are given in Table 1. The computation has been done for a temperature $T_{\text{mag}} = 0\,^\circ$C, and with $v_{\text{lim}} = 3.3 \times 10^4$ m•s^{-1}, as for the NMS MCP. The values have been normalized to the yield of the 3050 eV N_2^+ reference ions. Still, one may question the validity of using the NMS MCP coefficients a_k, b_k and v_{lim} for the DFMS MCP. One difference is the magnitude of the gain potential. Ions that enter the MCP pores are retarded by the MCP potential, reducing their impact velocity. This effect is more pronounced for larger gain potentials, but relatively speaking it remains below 5 % [31], so the fact that both MCPs work with different (and variable) gain potentials does not really matter. If the MCP operating conditions do not matter, the yields can change only because of the differences in MCP material. A change in MCP material is expected to affect the electron yields in a species-independent way, at least in a first approximation. Therefore the effects on relative yields have been evaluated when modifying v_{lim} (which is the same for all species), and when modifying the a_k and b_k by a common factor. The changes $\delta_v \mu_k$ in the relative yields as a consequence of changing v_{lim} by 25 % go from 2 % at low masses up to 5 % at $m_0 = 44$ Da; the changes are more important at high masses for which the ion velocity is closer to v_{lim}. The changes $\delta_b \mu_k$ from varying the b_k coefficients over a 25 % range go up to 20 %. Changing the a_k by a factor does not modify the relative yields at all. These considerations thus suggest that the μ_k are plausible approximations as they are not very sensitive to the systematic changes in the coefficients that accompany a change in MCP material. A comparison of the NMS MCP yields with those for different target materials revealed differences of less than 30 %, prompting a similar conclusion [31].

Table 1 also lists $\widehat{\mu}_k$ and $\tilde{\mu}_k$ as computed from Eqs. (24) and (25), the former for ions with $v_k \geq 4 v_{\text{lim}}$, the latter for ions with $v_{\text{lim}} \leq v_k \leq 4 v_{\text{lim}}$. While the values follow the overall decreasing trend of the μ_k with increasing mass, there are marked differences. Some can be attributed to the chemical identity of the impacting ions (e.g., for the sulphur-bearing compounds); secondary electron emission tends to be sensitive to the nature of the ions [e.g. Ref. [28]. Also, Eqs. (24) and (25) are good approximations for very large or small velocities, while they are used here at intermediate velocities.

DFMS laboratory calibration data obtained in the CASYMIR test facility [35] and reported in Ref. [21] are exploited here to verify the relative secondary electron yields. These calibration measurements aimed at establishing the sensitivities S''_j of a number of interesting neutral species to provide the information necessary for translating the R_k observed for the fragments directly into parent densities n_j via Eq. (17), thereby bypassing the need for the relative secondary electron yields. These calibration data contain sensitivity measurements for the MCP/LEDA, the channel electron multiplier (CEM), and the Faraday cup (FAR) sensors that were all part of the DMFS detector [1]. The CEM and FAR sensors were only used for calibration purposes. Obtaining accurate sensitivities proved to be challenging. The analysis below is therefore simplified, but in such a way that it provides an estimate of the uncertainty on the result. The basic assumption is that the fragmentation pattern is dominated by a single ion or, if multiple ions matter, that these have similar yields. For instance, H_2O, N_2 and CO_2 are species with a single dominant ion (their parent ion H_2O^+, N_2^+ and CO_2^+ respectively). A species having multiple fragments with similar yields is methane, with principal ions CH_4^+ and CH_3^+; because of the addition formula Eq. (21) the difference between the yields of both species must be less than 25 % since they differ by only one H atom. With the single-ion assumption the MCP/LEDA sensitivity satisfies

Table 1
Properties of electron impact ionization product ions in DFMS at $T_{mag} = 0^{\circ}$C: mass m, acceleration and total voltage V_{accel} and $V_{total} = V_{accel} + V_{post-accel}$, ion velocity v upon impact on the MCP, relative secondary electron yield μ computed with the parameters from [31, Table 2] and normalized to 3050 eV N_2^+ ions, change $\delta_v\mu$ when varying v_{lim} by 25%, change $\delta_b\mu$ when varying b by 25%, relative yield $\widehat{\mu}$ for light species (high velocities) from Eq. (24) and normalized so that $[\widehat{\mu}(N_2^+)/\widehat{\mu}(N_2^+\text{reference})]^2 = V_{total}(N_2^+)/V_{total}(N_2^+\text{reference})$, relative yield $\tilde{\mu}$ for heavier species (low velocities) from Eq. (25) and normalized with $\tilde{\mu}(N_2^+) = \widehat{\mu}(N_2^+)$, and relative secondary electron yields μ^{cal} with uncertainties $\delta\mu^{cal}$ computed from measurements [21] for the given calibration species, normalized so that $\langle\mu_k^{cal}/\mu_k\rangle = 1$.

Ion	m [Da]	V_{accel} [V]	V_{total} [V]	v [m·s^{-1}]	μ	$\delta_v\mu$	$\delta_b\mu$	$\widehat{\mu}$	$\tilde{\mu}$	μ^{cal}	$\delta\mu^{cal}$	Calibration species
N_2^+ reference	28.0056	3000.0	3050.0	144970	1.00	AS not convert	±0.00					
N^+	14.0025	4250.3	4300.3	243440	0.99	±0.02	±0.02	1.68				
O^+	15.9944	3719.0	3769.0	213240	1.04	±0.01	±0.05	1.47				
CH_4^+	16.0308	3719.0	3769.0	213000	1.26	±0.03	±0.20	1.47		0.69	±0.31	CH_4
NH_3^+	17.0260	3500.2	3550.2	200590	1.13	±0.01	±0.04	1.38				
H_2O^+	18.0100	3305.8	3355.8	189620	1.06	±0.01	±0.09	1.31		1.58	±0.28	H_2O
CO^+	27.9944	2125.1	2175.1	122450	0.59	±0.03	±0.08	0.84	0.84			
$C_2H_4^+$	28.0308	2125.1	2175.1	122370	0.58	±0.04	±0.10	0.84	0.84	0.65	±0.19	C_2H_6
										0.59	±0.07	C_2H_4
N_2^+	28.0056	2125.1	2175.1	122420	0.78	±0.02	±0.02	0.84	0.84	0.85	±0.19	N_2
$C_2H_5^+$	29.0386	2051.9	2101.9	118180	0.57	±0.04	±0.10		0.77	0.38	±0.09	C_3H_8
NO^+	29.9974	1983.5	2033.5	114370	0.67	±0.03	±0.05		0.72			
S^+	31.9715	1859.5	1909.5	107360	0.35	±0.03	±0.06		0.61			
O_2^+	31.9893	1859.5	1909.5	107330	0.57	±0.04	±0.07		0.61			
H_2S^+	33.9872	1750.1	1800.1	101100	0.35	±0.03	±0.06		0.53			
$C_3H_7^+$	43.0542	1383.8	1433.8	80165	0.31	±0.05	±0.06		0.29	0.35	±0.11	C_4H_{10}
CO_2^+	43.9893	1352.4	1402.4	78434	0.34	±0.05	±0.05		0.27	0.55	±0.17	CO_2

$$S''^{MCP}_X = S_X\,\tau_{X^+}\,\gamma_{X^+}, \tag{27}$$

with γ_{X^+} the absolute yield of the dominant ion(s). The CEM sensitivities were also obtained, but with the CEM operating in digital counting mode. It is assumed that the secondary electron yield upon ion impact in the CEM is sufficiently high so as to be able to ignore the fraction of events ($e^{-\gamma_{CEM}}$) for which an ion does not produce any electrons. Counting electron pulses then is the same as counting ions (justified to the 1 % level if $\gamma_{CEM} \geq 4.6$). The CEM sensitivity therefore is

$$S''^{CEM}_X = S_X\,\tau_{X^+}. \tag{28}$$

Consequently, the yield can be found from

$$\gamma_{X^+} = \frac{S''^{MCP}_X}{S''^{CEM}_X}. \tag{29}$$

In principle the same can be done with the FAR sensitivities, but because of low signal these values could not (reliably) be derived. The MCP/LEDA and CEM sensitivities were obtained in the low and high mass resolution modes, and for $I_{em} = 2$, 20 and 200 μA. It is assumed that the fragmentation patterns do not change significantly with I_{em} [21]. Following Eq. (29) one has 6 estimates of γ_{X^+} from which the average $\gamma^{cal}_{X^+}$ and the standard deviation $\delta\gamma^{cal}_{X^+}$ are determined. Since the set of calibrated species did not include the reference species at the reference energy, the relative yields $\mu_k^{cal} = \gamma_k^{cal}/\gamma^*$ were obtained by finding γ^* from

$$\frac{\sum_k w_k\gamma_k^{cal}\big/\mu_k}{\sum_k w_k} = \gamma^*\frac{\sum_k w_k\mu_k^{cal}\big/\mu_k}{\sum_k w_k} = 1, \tag{30}$$

where the $w_k = 1/(\delta\gamma_k^{cal})^2$ act as weights and the sum covers all the species for which the calibration measurement has been done. Table 1 lists $\mu_k^{cal} = \gamma_k^{cal}/\gamma^*$ and $\delta\mu_k^{cal} = \delta\gamma_k^{cal}/\gamma^*$. The $\delta\mu_k^{cal}$ are rather high, highlighting the difficulty of the sensitivity measurements. Despite the simplified derivation and the measurement errors, the μ_k^{cal} reasonably match the μ_k.

Since the framework put forward in Ref. [31] forms a consistent picture that can be applied to a variety of species (also species that have not been measured in the laboratory because they require special precautions, such as CO, HCN, HF which are poisonous or

Table 2
Double Gaussian fit parameters as a function of commanded mass-over-charge $_+m_0$ obtained at times when $T_{mag} \in [-3, +1]^{\circ}$C during 15–30 October 2014: the half-widths w_1 and w_2 of the primary and secondary Gaussian components, and the relative contribution α of the secondary Gaussian, for LEDA channels A and B. The margins indicate the range of variability of the parameters at the 1 σ level. The last line gives the weighted averages of the fit parameters. The parameters were obtained by fitting all peaks (including overlapping species) in each spectrum with the same peak shape.

m_0[Da]	w_{1A}[pixels]	w_{1B}[pixels]	w_{2A}[pixels]	w_{2B}[pixels]	α_A	α_B
16		3.59±0.18	7.75±0.38	8.40±0.53	0.08±0.02	0.08±0.01
17		3.43±0.17	7.96±0.32	8.50±0.36	0.09±0.02	0.09±0.01
18		3.29±0.09	7.55±0.36	8.15±0.32	0.08±0.01	0.08±0.01
19		3.55±0.17	9.27± 2.04	9.48±1.04	0.06±0.02	0.08±0.02
20		3.75±0.16	8.50±2.25	8.90±2.44	0.07±0.04	0.08±0.04
28		3.46±0.19	8.53±0.57	7.95±0.41	0.07±0.01	0.08±0.01
32		3.36±0.12	8.11±0.24	7.88±0.37	0.09±0.01	0.10±0.01
35		3.65±0.28	6.17±3.40	6.31±3.16	0.09±0.05	0.09±0.05
36		3.53±0.15	7.94±1.71	7.88±1.45	0.10±0.04	0.11±0.04
37		3.61±0.22	6.41±0.90	6.87±0.99	0.13±0.04	0.13±0.04
38		3.73±0.20	4.81±1.05	5.74±1.28	0.11±0.06	0.13±0.05
44		3.83±0.19	8.19±0.22	8.17±0.37	0.10±0.01	0.09±0.02
Average		*3.49±0.05*	*7.95±0.15*	*8.12±0.14*	*0.09±0.01*	*0.09±0.01*

corrosive), since the μ_k are not too sensitive to the MCP material properties, and since they agree with the results from the calibration measurements in an overall sense, these values for the relative secondary electron yields will be used in what follows.

4. Peak shapes

The ion count rate calibration depends on the gain. The concept of modal gain relates to the total number of electrons that exit the MCP. For various reasons the distribution of those electrons over the pixels (the peak shape) is not always identical.

4.1. Typical peak shape

The peaks in the DFMS mass spectra can be represented by a double Gaussian shape [7,36]. A single Gaussian peak centred on pixel p^* with half-width w has a shape function

$$\varphi(p,p^*,w) = e^{-\frac{(p-p^*)^2}{w^2}}, \tag{31}$$

where p is the pixel number and where $\varphi(p^*,p^*,w) = 1$. A double Gaussian shape centred on pixel p^* then is

$$\psi(p,p^*,w_1,w_2,\alpha) = (1-\alpha)\varphi(p,p^*,w_1) + \alpha\varphi(p,p^*,w_2), \tag{32}$$

where w_1 and w_2 represent the half-widths of both Gaussians ($w_2 > w_1$) and where $0 \leq \alpha < 1$ is the relative contribution of the second Gaussian; again, $\psi(p^*,p^*,w_1,w_2,\alpha) = 1$. For such a double Gaussian, the area is

$$\Psi = \sqrt{\pi}[(1-\alpha)w_1 + \alpha w_2]. \tag{33}$$

The double Gaussian shape can be applied to peaks in the raw spectra (as is done here), where the independent variable is the LEDA pixel number, or to the calibrated spectra, where the independent variable is mass-over-charge [36]. There is a slight difference between both because mass is not exactly linearly proportional to pixel number (see Eq. (1)); however, over the width of a single peak this difference is negligible.

4.2. Origin of the peak shape

Laboratory experiments have been performed with very narrow ion beams hitting the MCP/LEDA assembly and measuring the resulting peak shape [7], which also turns out to be a double Gaussian. The primary Gaussian stems from the manner in which the electrons are produced in the MCP pores [e.g., Refs. [37,38]] and how they traverse the 0.2 mm gap between MCP and LEDA. When an ion hits the wall of a pore close to the MCP front, it ejects a number of electrons (secondary electron yield). These electrons cover a range of ejection angles and energies, depending on the incident ion momentum and the structural arrangement of the atoms in the pore wall [39]. These electrons are accelerated because of the MCP voltage difference to energies ranging from several to a few hundred eV before hitting the wall again and producing even more electrons [7]. This random process repeats and at the MCP pore exit the electron energy and angular distributions have become Gaussian. A potential difference of ~ 200 V between the MCP back and the LEDA [1] accelerates the electrons towards the LEDA to achieve a certain degree of focusing [7]. As these electrons hit the LEDA with sufficient energy, they may in turn eject secondary electrons, which are attracted back to the LEDA because of the potential difference, thus forming the secondary Gaussian [7,16].

We have conducted simulations in which the electron cascade double Gaussian distribution ψ is characterized by half-widths $w_{e1} = 2.5$ pixels and $w_{e2} = 5.0$ pixels, and by $\alpha_e = 0.10$, and where the pulse height has a normal distribution with a standard deviation that is 0.20 times the modal gain. If the intensity distribution in the ion beam is Gaussian with a spread of only $w_i = 0.5$ pixel$\ll w_{e1}$, then all ions arrive at approximately the same spot on the MCP. The mass peak resulting from the convolution of the Gaussian ion distribution and the double Gaussian electron cascade distribution can in turn be represented by a double Gaussian, with $w_1 = 2.55$ pixels$\approx w_{e1}$, $w_2 = 4.95$ pixels$\approx w_{e2}$, and $\alpha = 0.12 \approx \alpha_e$, essentially the shape of the electron cascade (Fig. 2, top left). If the ion beam is broader, $w_i = 2.5$ pixels, the net distribution can still be approximated by a double Gaussian, but with different parameters ($w_1 = 4.3$ pixels, $w_2 = 6.1$ pixels, $\alpha = 0.15$; Fig. 2, bottom left).

4.3. Peak shape changes due to finite sampling

The peaks in Fig. 2 (left) were obtained by accumulating the electron distributions for $N_{\text{ion}} = 5000$ ions, randomly generated following a Gaussian ion beam intensity profile and a normally distributed pulse height, which is sufficiently large to obtain symmetric peaks. For less intense peaks the shape can be different because of the discrete nature of peak build-up. Fig. 2 (right) shows examples for the same ion beam widths, but with $N_{\text{ion}} = 20$ ions. Peak shape deviations show up more readily when $w_i \geq w_{e1}$. A first consequence is that the centre of the peak might be slightly off the true position. One must therefore be prudent to use peaks of weakly abundant ions for mass calibration or species identification. A second consequence is that peak height may vary while peak area (which represents the total number of electrons) remains constant. Using peak height as an indicator for peak intensity (calibration option 1) may therefore lead to minor errors, while it is more advisable to use peak area (options 2 and 3).

The double Gaussian fit parameters have been determined as a function of N_{ion} for an ensemble of random realizations of the measurement process. The top panel in Fig. 3 shows, for $w_i = 2.5$ pixels, how the peak position established from a double Gaussian fit tends to approximate the true peak position within ± 0.5 pixels only for $N_{\text{ion}} > 200$. The peak height-over-area ratio h/A evolves from $1/\sqrt{\pi}[(1-\alpha_e)w_{e1} + \alpha_e w_{e2}] = 0.205$ at $N_{\text{ion}} = 1$ (the value for the electron cascade distribution) to a constant value for large N_{ion}. The ratio is well-determined down to 5% only for $N_{\text{ion}} > 500$ (precise value depends on ion beam width). Using peak area thus offers a distinct advantage over peak height, especially for less abundant species. Note that peak centre and peak area can be improved on by adding successive spectra, thus increasing N_{ion} at the expense of time resolution; however, this is only possible if the mass calibration is accurately known and the signal source is stable.

4.4. Peak shape changes due to a variable electron cascade

The shape of the electron cascade depends on the potential difference between the MCP back surface and the LEDA [7]; this was kept fixed in DFMS. The shape of the electron cascade can change when the MCP gain changes, as this affects the electron energy distribution at the MCP pore exit, but this is expected to be minor. The acceleration potential in the mass spectrometer is strongly dependent on m_0, so that heavier ions reach the MCP with less energy, which affects the sensitivity but does not change the electron cascade shape.

MCP gain depends slightly on temperature. A gain variation of $< 0.2\%\ (^\circ\text{C})^{-1}$ is typical [e.g. Refs. [40,41]]; the gain decreases somewhat with temperature as a consequence of the thermal gradient in the MCP pores in combination with the exponential temperature dependence of the MCP resistivity. Any effect on the

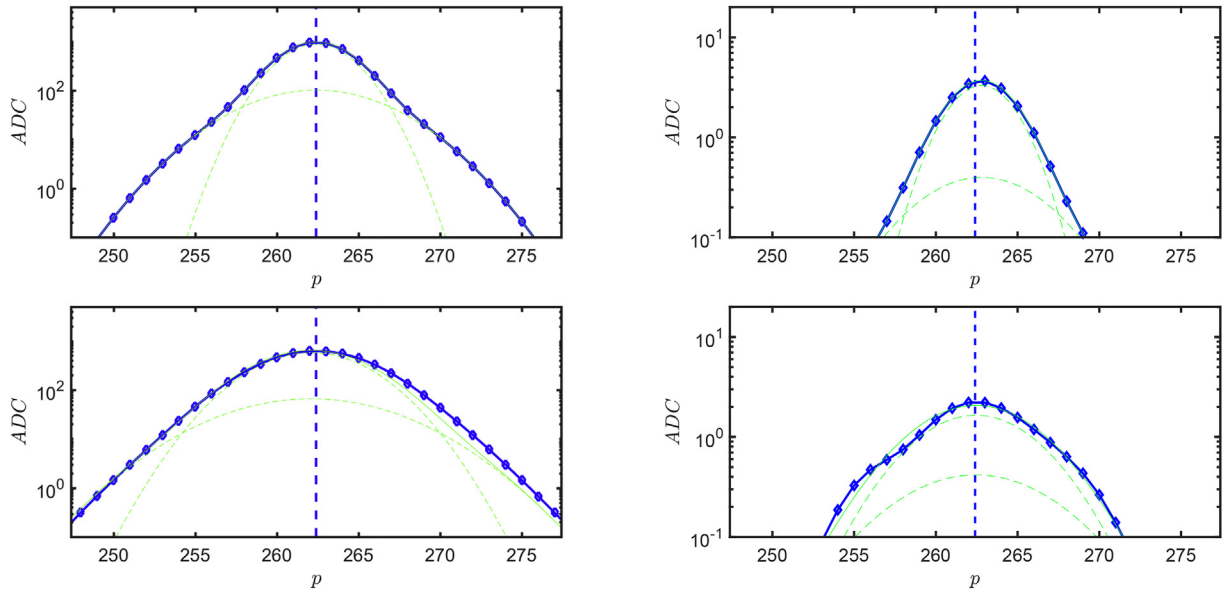

Fig. 2. Simulated LEDA electron distributions obtained by accumulating the electron cascade (double Gaussian with half-widths $w_{e1} = 2.5$ pixels and $w_{e1} = 5.0$ pixels, relative contribution of the secondary Gaussian $\alpha_e = 0.05$, pulse height distribution standard deviation 20 %) for $N_{\text{ion}} = 5000$ ions (left) and for $N_{\text{ion}} = 20$ ions (right), assuming a Gaussian intensity distribution in the ion beam with (top) $w_i = 0.5$ pixels and (bottom) 2.5 pixels. The exact peak location is at pixel $p = 262.4$. The intensity scale is proportional to the ADC counts the LEDA would record, normalized so that the area under the peak equals N_{ion}. The measurements are shown in blue. The double Gaussian fits are plotted as solid green lines, with both components as dashed green lines. (For interpretation of the references to colour in this figure legend, the reader is referred to the Web version of this article.)

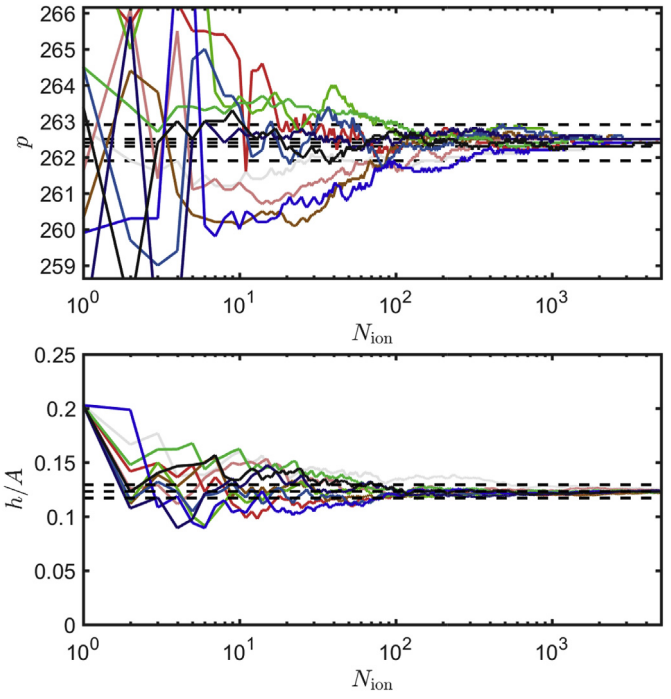

Fig. 3. Peak centre position p (top) and peak height-over-area ratio h/A (bottom) for an ion beam half-width $w_i = 2.5$ pixels (electron cascade double Gaussian with $w_{e1} = 2.5$ pixels and $w_{e1} = 5.0$ pixels, and $\alpha_e = 0.05$) as a function of N_{ion}. The plots show 10 random realizations of the measurement process, as indicated by the various colours. The horizontal dashed lines show limits of ±0.1 and ±0.5 pixels around the nominal peak position at pixel $p = 262.4$ (top) and of ±5 % around the limit value for h/A (bottom). (For interpretation of the references to colour in this figure legend, the reader is referred to the Web version of this article.)

shape of the electron cascade at the MCP exit can therefore also be expected to be minor. As the temperature variations in the MCP/LEDA detector assembly vary between −25 °C and + 15 °C, the effect is at most 4%. In view of other sources of uncertainty, no such gain variation with temperature is taken into account in the calibration process. Rescaling the ion fluxes to match the COPS density may correct for such MCP gain variations to the extent that MCP temperature and gas composition remain constant during a mass scan.

To evaluate the influence of the electron cascade width on the overall peak shape, computations were carried out to determine the double Gaussian peak parameters that result from the convolution of an ion beam with a width of $w_i = 2.5$ pixels and an electron cascade with varying half-widths w_{e1} and $w_{e2} = 2w_{e1}$, with $\alpha_e = 0.10$ and for $N_{\text{ion}} = 5000$. Fig. 4 (left) shows that, as long as $w_{e1} \gg w_i$, the resulting peak has $w_1 \approx w_{e1}$, $w_2 \approx w_{e2}$, and $\alpha \approx \alpha_e$. For smaller w_{e1}, $w_1 \approx w_i$ and thus $w_2/w_1 < w_{e2}/w_{e1}$. In general, α is the parameter that is the most difficult to determine precisely. In all these cases the area under the double Gaussian fit represents the true area under the peak very well ($Q \approx 1$).

4.5. Peak shape changes due to variable ion beam dispersion

Fig. 4 (right) shows how the resulting beam shape depends on the ion beam width: The broader the ion beam, the broader the resulting beam. This is most readily visible in w_1 and to a lesser extent in w_2, so that the ratio w_2/w_1 progressively decreases, while α increases. The area under the double Gaussian fit increasingly deviates from the true area under the peak ($Q \neq 1$); the resulting beam can no longer be well represented by a double Gaussian as soon as $w_i > 1.5\, w_{e1}$.

Table 2 summarizes the double Gaussian peak fit parameters for all DFMS high resolution mass spectra obtained during 15–30 October 2014, whenever the magnet temperature was in the $[-3, +1]$ °C range. All peaks on a given spectrum were fitted with the same double Gaussian shape; the parameters defining that shape are given in the table. The preprocessing technique demonstrated in Ref. [36] has been applied to the $m_0 = 16, 17, 18$ Da spectra to eliminate an instrumental problem. The data include spectra collected with a variety of gain steps. The spread on the fit

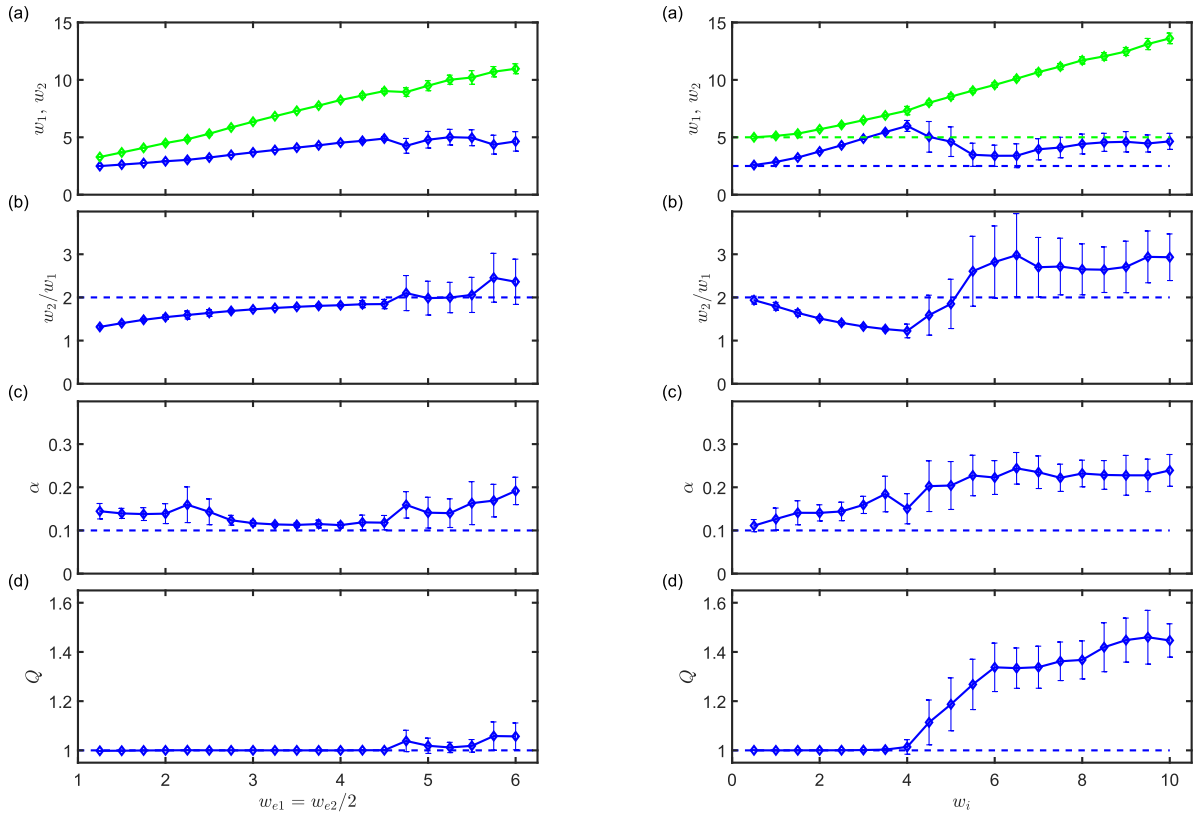

Fig. 4. Variations of the double Gaussian peak shape parameters (left) for different electron cascade widths ($w_{e2} = 2w_{e1}$, $\alpha_e = 0.10$) and fixed ion beam width ($w_i = 2.5$ pixels), and (right) for different ion beam widths and fixed electron cascade width ($w_{e1} = 2.5$ pixel, $w_{e2} = 5$ pixel, $\alpha_e = 0.10$): (a) primary half-width w_1, (b) secondary half-width w_2, (c) relative contribution of the secondary Gaussian α, and (d) the ratio Q between the actual and the fitted peak area. The error bars correspond to 1 σ bounds derived from repeating the measurement simulation a large number of times.

parameters (in part reflecting the quality of the fitting procedure) is small for well-defined peaks (H_2O, CO, O_2 and CO_2 at $m_0 = 18, 28, 32, 44$ Da), indicating that the gain step has no noticeable effect on peak shape. Therefore either the change in the electron cascade properties is negligible, or the ion beam width is broader ($w_i > w_{e1}$). The fit parameters vary slightly with m_0, with w_1 and w_2 showing a similar variation, suggesting that the ion optics is responsible for these changes and that the peak width is dominated by the ion beam width.

The peak shape in high resolution mode obviously depends on the ion zoom optics, which uses a hexapole and two quadrupoles [1]. The electric potentials steering these ion lenses depend on commanded mass-over-charge. As they can only be commanded with a finite precision, they contribute to a variable ion beam dispersion.

The peak fit parameters for the spectra at $m_0 = 18$, 28, 32 and 44 Da are shown as a function of time for October 2014 in Fig. 5, but now without the temperature restriction. In general, w_1, w_2 and α show variations with the temperature of the ion optics; this is best visible for $m_0 = 44$ Da. These parameters correlate better with T_{mag} than with T_{LEDA}, confirming the importance of the ion optics. As DFMS resumes operation after being shut down, it is heated up by the instrument electronics so that T_{mag} increases from around -10°C to its nominal value of $\sim 0^\circ$C. The low-temperature spectra are characterized by a sharpening of the peaks for CO (w_1 decreases by 10%, w_2 by up to 20%) and a broadening for CO_2 (w_1 and w_2 increase by 15%); an example of the latter is presented in Fig. 1. It can be concluded that the ion beam is affected by temperature-related changes in the ion optics (e.g., thermal deformation of the structure, change of magnetic fields in the permanent magnet, limited precision commanding of the instrument potentials) resulting in a modification of peak shape that depends on commanded mass-over-charge.

4.6. Peak shape differences between LEDA channel A and B

Comparing the mass peaks recorded by LEDA channel A and B, one finds that the half-widths w_1 and w_2 on channel B tend to be a little larger (see Table 2). Note that there also is a peak position offset of a few pixels between peaks recorded in both channels, as can be seen in Fig. 1; the offset is 3 pixels at most. Fig. 6 sketches the LEDA with both anode rows and the footprint of the ion beam. The interpretation is that the focal alignment is not perfect, causing a small shift in peak position and an additional broadening of the peaks. If the peak positions on both LEDA rows differ by 1 pixel, the misalignment is only

$$\theta = \arctan\frac{x}{2y} \approx 0.09^\circ, \tag{34}$$

where $x = 25$ μm is the pixel width and $y = 8$ mm the pixel height (ignoring the small separation between row A and B and between the pixels). Such a misalignment adds about 0.5 pixel to the peak half-width. It is therefore plausible to conclude that $w_{e1} \approx 1.5$ pixel and that $w_i \approx 2$ pixel (by design compatible with w_{e1}), resulting in a combined peak width of ~ 3 pixel, which is degraded by the misalignment to an effective primary peak width of ~ 3.5 pixel. A slight curvature or a broadening of the beam cross section can explain why the width on row B is a little larger, and why α may be somewhat different.

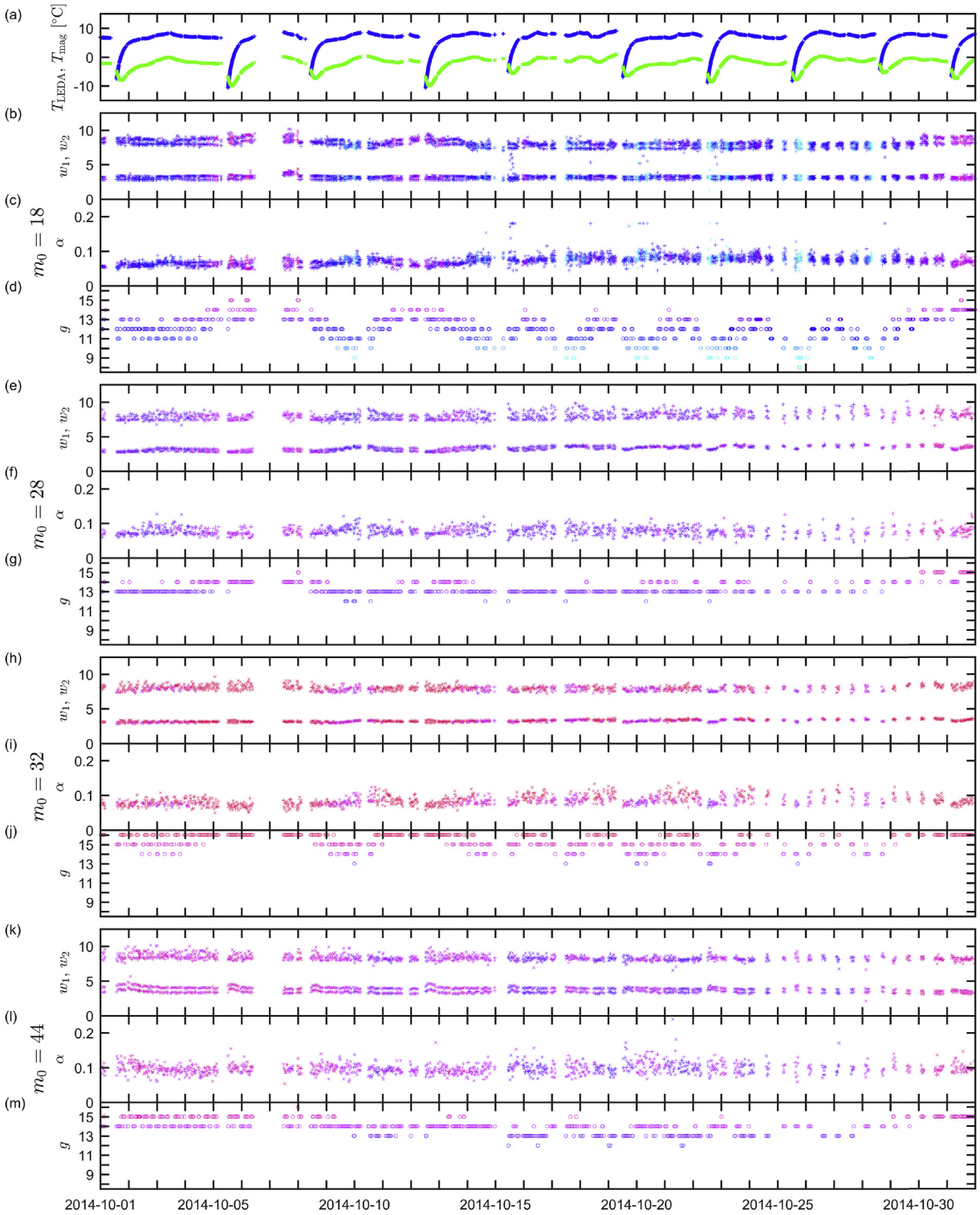

Fig. 5. Peak fit parameters for October 2014 showing (a) LEDA and magnet temperature in blue and green respectively; (b–d) half-widths of the primary and secondary Gaussian peak shape components, w_1 and w_2, and relative contribution of the secondary component, α, in spectra for commanded mass-over-charge $m_0 = 18$ Da; (e–g) for $m_0 = 28$ Da; (h–j) for $m_0 = 32$ Da; (k–m) for $m_0 = 44$ Da. The data points are colour-coded according to the gain step g, with + symbols for channel A and × for channel B. (For interpretation of the references to colour in this figure legend, the reader is referred to the Web version of this article.)

5. Comparison of calibration options

As has amply been demonstrated in the previous section, the peak shape changes because of thermal transients and also, for many interesting minor species, because of limited count rates. To compensate for the effects of peak shape changes, the following ion count rate calibration procedure is used:

1. First, the mass scale of the raw spectrum is calibrated.

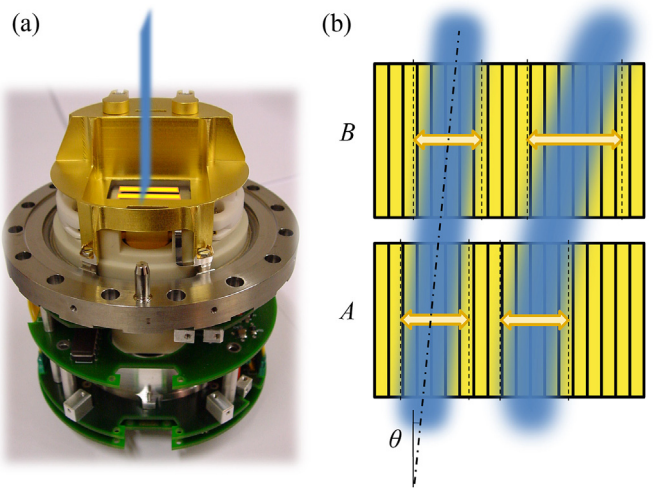

Fig. 6. Schematic view of the LEDA detector array and the ion beam footprint. (a) EQM model of the DFMS detector unit with the focused ion beam in blue and the LEDA detector chip anode rows in yellow. (b) Top view of the LEDA detector showing how a misalignment angle θ gives rise to an ion beam position difference between row A and B and an increase of the width on each individual row; a curvature of the beam cross section can explain the width differences between both rows. Photograph courtesy of J. M. Iliano. (For interpretation of the references to colour in this figure legend, the reader is referred to the Web version of this article.)

2. The position-dependent gain correction is applied following Eq. (3) [16].
3. The intensity scale is calibrated using Eq. (4) to obtain the spectrum $\widehat{R}(p)$ with calibration option 1.

4. Double Gaussian fits are computed for all peaks in the spectrum. Using the same peak shape $\psi(p)$ for all peaks in the spectrum is an adequate choice that facilitates fitting low-intensity peaks and peaks that are superposed on adjacent peaks of more abundant species. Note, however, that for low ion count rates, fitting a variable double Gaussian shape may still not be very precise, but it is adequate since the error due to poor counting statistics then dominates anyhow.

5. For each of these peaks, with maximum at pixel position p_k, the area is computed as $A_k = \widehat{R}(p_k, g, t)\,\Psi_k$. If the gain factor has been evaluated based on peaks with a shape $\psi^*(p)$ and an integrated area $A^* = \Psi^*$, the ion count rate can be found as

$$\mathscr{R}_k = \frac{R_k}{\mu_k} = \frac{1}{\mu_k}\frac{A_k}{A^*} = \frac{\widehat{R}(p_k, g, t)}{\mu_k}\frac{\Psi_k}{\Psi^*} \tag{35}$$

which follows calibration option 2. The peak shape used during the gain measurements and its dependence on m_0 are not known in detail. Taking the averages given in Table 2 as a reference, one finds that $\Psi^*_A = 6.639$ and $\Psi^*_B = 6.924$. The reference values carry some uncertainty, within the uncertainty on the gain. Note that the reference values cancel out when determining relative variability or ratios of ion count rates, or when normalizing the data relative to the total gas density observed by COPS.

Fig. 7 shows the ion count rates for H_2O^+, CO^+, O_2^+ and CO_2^+ for October 2014. The ratio of ion count rates based on peak area and on peak height, Ψ/Ψ^*, changes with each temperature transient. For CO_2^+, Ψ/Ψ^* increases at low temperature, while $\Psi/\ \Psi^*$ decreases for CO^+ and O_2^+. For H_2O^+, Ψ/Ψ^* is fairly constant thanks to the preprocessing technique [36].

The Ψ/Ψ^* variations sometimes reach up to $> 20\,\%$, leading to significant differences in ion count rates obtained with option 1 and 2, although these may appear small in view of the large diurnal variations. While the instrument shut-down periods are relatively short, it takes a long time for DFMS to recover to its nominal temperature, in part due to the high thermal inertia of the magnet. Therefore, about 25% of the time is spent outside the $[-3, +1]^\circ$C interval. Option 2 is therefore a necessity for establishing long-term averages. It has therefore been used for the provision of the ROSINA DFMS Level 5 data in ESA's Planetary Science Archive.

Relative ion count rates are often directly proportional to the relative abundances of the corresponding parent species. When computing such relative quantities, several systematic errors disappear, such as the uncertainty on the gain associated with the definition of Ψ^*. Because the trends of the Ψ variation with temperature may have opposite directions for different ions, the net effect on ion count rate ratios can be considerable. Fig. 8 shows the ratios relative to H_2O^+.

6. Conclusion

The Double Focusing Mass Spectrometer (DFMS) on the Rosetta spacecraft is a complex instrument. Its behaviour depends on its thermal state as temperature controls the magnetic field strength, the MCP gain, etc. Instrument temperature varies with illumination and with self-heating by the electronics. Large temperature variations are associated with instrument shut-down and restart after thruster operations. This temperature dependence results in changes in the shape of the mass peaks obtained in neutral mode. It has been shown that this can lead to errors of up to 20% on the ion count rates if this is not accounted for. In that case one would obtain ion count rates that may be systematically too low or too high during the low-temperature transients whenever DFMS is restarted. Given the frequency with which these occur and the time needed to recover to the nominal temperature, this may cause systematic deviations even if long-term averages are used. Such systematic errors may be even worse when considering ion ratios or abundance ratios of neutral species computed from them. Note that while DFMS is off, its source continues to collect icy dust grains and to act as a cold trap for comet gas, explaining why an enhanced background is measured as the source warms up after restart.

Accounting for peak shape changes is also important for species that have low abundance. While for abundant species the overall peak can be modelled very well as a double Gaussian, this is not the case for minor species, in particular when the secondary Gaussian component disappears in the noise. By considering peak area rather than peak height, different peak shapes can be accounted for. However, in such situations the error is invariably large: The arrival of ions at the MCP/LEDA detector can be regarded as a discrete stochastic Poisson process in time, so that the standard deviation on an accumulated ion count $N_{\mathrm{ion}} = (\mathscr{R}/\mu)\,\Delta t = R\,\Delta t$ is $\sqrt{N_{\mathrm{ion}}}$, and the relative error is $1/\sqrt{N_{\mathrm{ion}}}$, which is below 10 % only if $N_{\mathrm{ion}} > 100$ (given that μ is of order unity). For DFMS, which accumulates spectra during $\Delta t = 19.66$ s, that amounts to ion count rates $R > N_{\mathrm{ion}}/\Delta t \approx 5$ ions$\cdot$s^{-1}.

The mass peak parameters clearly correlate with magnet temperature T_{mag}, confirming that the ion optics is responsible for this temperature-dependent behaviour. The peak shape parameters can be described by a linear function of T_{mag} with the fit coefficients depending on m_0. Such linear approximations can be used to fix these parameters, or to constrain them more narrowly, to make peak fitting faster and more robust, especially when dealing with peaks of minor species superposed on the flanks of peaks of more abundant species.

The procedure described in this paper helps to eliminate an important source of systematic error on the ion count rates. Apart from the Poisson counting statistical error, the major error sources

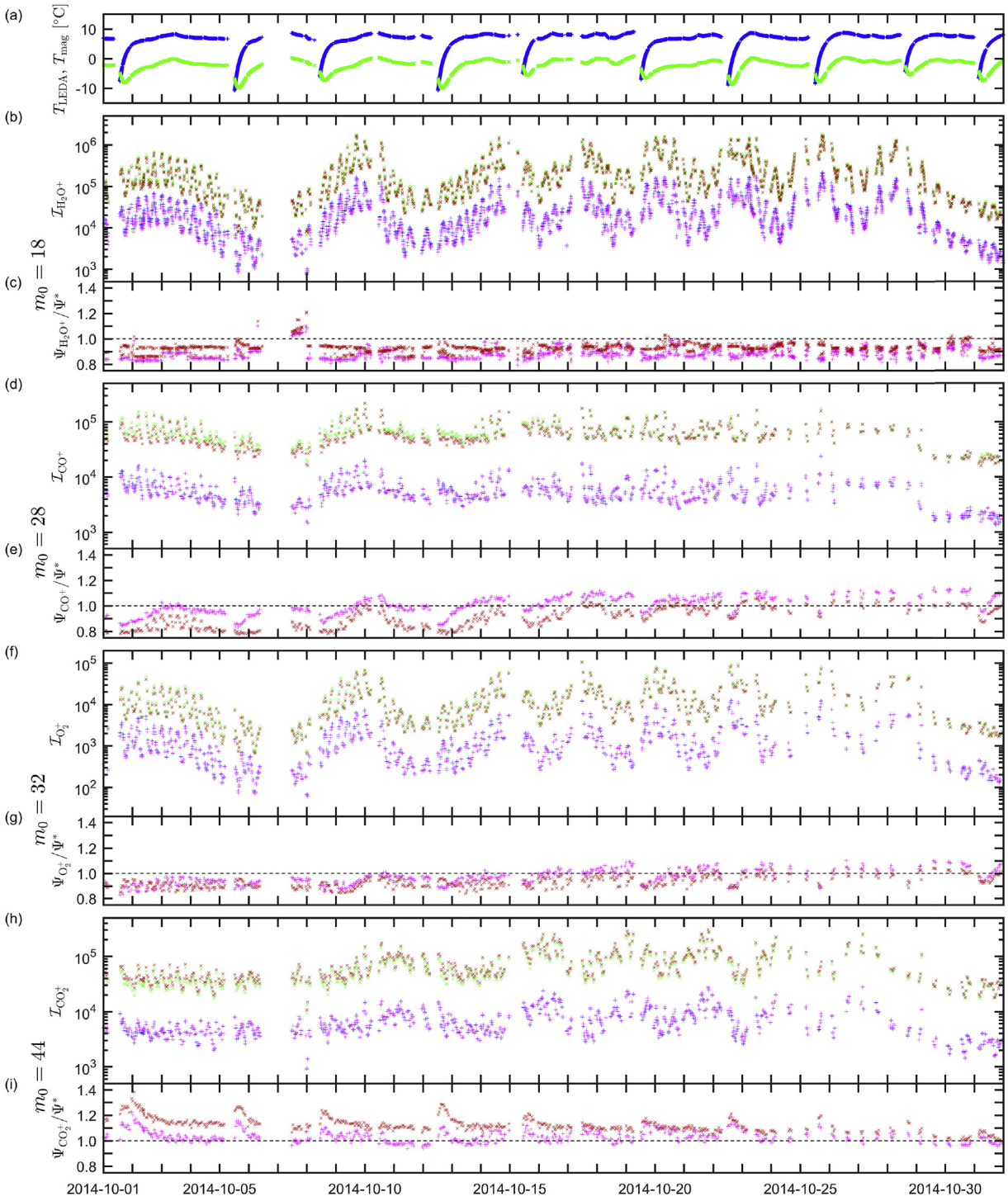

Fig. 7. Ion count rates for October 2014. (a) LEDA and magnet temperature in blue and green respectively. Ion count rates are given for (b–c) H_2O^+, (d–e) CO^+, (f–g) O_2^+ and (h–i) CO_2^+. Count rates for channel A are indicated with + symbols, in blue for the count rates based on peak height, magenta for the count rates based on peak area; count rates for channel B are indicated with × symbols, in green and red for count rates based on peak height and area, respectively. The count rates for channel B have been multiplied by 10 to improve figure readability. The ratio of both count rates, Ψ/Ψ^*, varies with instrument temperature; while it is rather constant for H_2O^+, it tends to increase at low temperature for CO_2^+ but decreases for CO^+ and O_2^+. (For interpretation of the references to colour in this figure legend, the reader is referred to the Web version of this article.)

are the uncertainty on the relative secondary electron yields, believed to be below 50% for the most relevant species in the comet atmosphere, and the uncertainty on the gain, in particular due to ageing of the detector. The latter is believed to be within 25%, given the position-dependent gain measurement procedure that has been performed regularly during the mission [see 15, supplementary material]. The ion count rates serve as inputs for recovering the parent densities with the help of the sensitivities and fragmentation patterns (*S*' and *F*'), which carry their own uncertainties that are often even more important, depending on whether laboratory calibration measurements are available. Any reduction of the uncertainty on the ion count rates leads to a

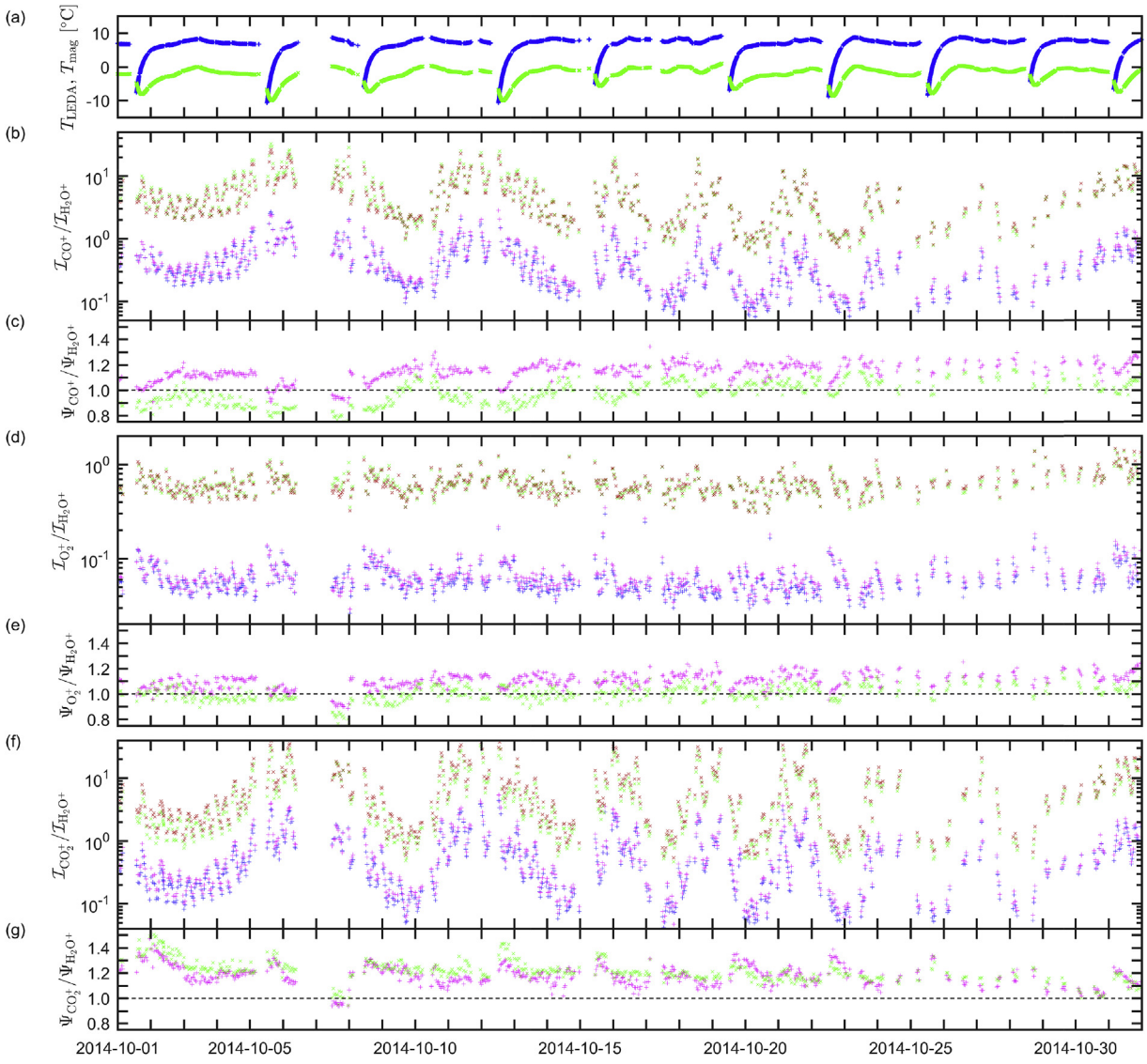

Fig. 8. Ion count rates relative to H_2O^+ for October 2014. (a) LEDA and magnet temperature in blue and green respectively. Relative count rates are given for (b–c) CO^+, (d–e) O_2^+ and (f–g) CO_2^+. Relative count rates for channel A are indicated with + symbols, in blue for the count rates based on peak height, magenta for the count rates based on peak area; relative count rates for channel B are indicated with × symbols, in green and red for count rates based on peak height and area, respectively. The relative count rates for channel B have been multiplied by 10 to improve figure readability. (For interpretation of the references to colour in this figure legend, the reader is referred to the Web version of this article.)

corresponding reduction of the uncertainties on the neutral species abundances. If sensitivities and fragmentation fractions incorporating the relative secondary electron yield (S" and F") are available, then there is no need to compute the ion count rates as such, since one can go directly from mass peak area for the parent and fragment ions to parent densities. In that case, the uncertainties associated with the Poisson counting error, the position-dependent gain, the sensitivity and the fragmentation pattern all combine to determine the uncertainty on the parent densities. An important part of this uncertainty can be removed by rescaling the densities relative to the total density as determined by the ROSINA COPS sensor.

Declaration of competing interest

The authors report no conflicts of interest in this work.

Acknowledgements and Funding

The authors thank the following institutions and agencies: Part of the work at BIRA-IASB was supported by the Belgian Science Policy Office, Belgium via PRODEX/ROSINA PEA 90020 and an Additional Researchers Grant (Ministerial Decree of 2014-12-19). AG thanks Fonds National pour la Recherche Scientifique (FNRS) for a FRIA research grant. Work at UoB was funded by the State of Bern, the Swiss National Science Foundation, Switzerland, and by the European Space Agency PRODEX Program. Work at Southwest Research institute, USA was supported by subcontract no. 1496541 from the Jet Propulsion Laboratory. Work at LATMOS has been carried out thanks to the support of the A*MIDEX project (nr. ANR-11-IDEX-0001-02) funded by the "Investissements d'Avenir" French Government program, managed by the French National Research Agency (ANR), and of CNES, France grants. Work at the University of Michigan was funded by NASA under contract JPL-1266313. The results from ROSINA would not be possible without the efforts of

the many engineers, technicians, and scientists involved in the mission and in the ROSINA instrument team over the past 20 years, whose contributions are gratefully acknowledged. Rosetta is an ESA mission with contributions from its member states and NASA. All ROSINA data are available from the PSA archive of ESA and the PDS archive of NASA. Data and software used to produce the tables and figures in this manuscript are available from the authors upon request.

Appendix A. Supplementary data

Supplementary data to this article can be found online at https://doi.org/10.1016/j.ijms.2019.116233.

References

[1] H. Balsiger, K. Altwegg, P. Bochsler, P. Eberhardt, J. Fischer, S. Graf, A. Jäckel, E. Kopp, U. Langer, M. Mildner, J. Müller, T. Riesen, M. Rubin, S. Scherer, P. Wurz, S. Wüthrich, E. Arijs, S. Delanoye, J. De Keyser, E. Neefs, D. Nevejans, H. Rème, C. Aoustin, C. Mazelle, J.-L. Médale, J.A. Sauvaud, J.-J. Berthelier, J.-L. Bertaux, L. Duvet, J.-M. Illiano, S.A. Fuselier, A.G. Ghielmetti, T. Magoncelli, E.G. Shelley, A. Korth, K. Heerlein, H. Lauche, S. Livi, A. Loose, U. Mall, B. Wilken, F. Gliem, B. Fiethe, T.I. Gombosi, B. Block, G.R. Carignan, L.A. Fisk, J.H. Waite, D.T. Young, H. Wollnik, Rosina - Rosetta orbiter spectrometer for ion and neutral analysis, Space Sci. Rev. 128 (1–4) (2007) 745801, https://doi.org/10.1007/s11214-006-8335-3.

[2] K. Altwegg, H. Balsiger, A. Bar-Nun, J.-J. Berthelier, A. Bieler, P. Bochsler, C. Briois, U. Calmonte, M. Combi, J. De Keyser, P. Eberhardt, B. Fiethe, S.A. Fuselier, S. Gasc, T.I. Gombosi, K.C. Hansen, M. Hässig, A. Jäckel, E. Kopp, A. Korth, L. Le Roy, U. Mall, B. Marty, O. Mousis, E. Neefs, T. Owen, H. Rème, M. Rubin, T. Sémon, C.-Y. Tzou, H. Waite, P. Wurz, 67P/Churyumov-Gerasimenko, a Jupiter family comet with a high D/H ratio, Science 347 (6220) (2014) 1261952, https://doi.org/10.1126/science.1261952.

[3] H. Balsiger, K. Altwegg, A. Bar-Nun, J.-J. Berthelier, A. Bieler, P. Bochsler, C. Briois, U. Calmonte, M. Combi, J. De Keyser, P. Eberhardt, B. Fiethe, S.A. Fuselier, S. Gasc, T.I. Gombosi, K.C. Hansen, M. Hassig, A. Jackel, E. Kopp, A. Korth, L. Le Roy, U. Mall, B. Marty, O. Mousis, T. Owen, H. Reme, M. Rubin, T. Semon, C.-Y. Tzou, J.H. Waite, P. Wurz, Detection of argon in the coma of comet 67P/Churyumov-Gerasimenko, Sci. Adv. 1 (8) (2015), https://doi.org/10.1126/sciadv.1500377 e1500377–e1500377.

[4] A. Bieler, K. Altwegg, H. Balsiger, A. Bar-Nun, J.-J. Berthelier, P. Bochsler, C. Briois, U. Calmonte, M. Combi, J. De Keyser, E.F. van Dishoeck, B. Fiethe, S.A. Fuselier, S. Gasc, T.I. Gombosi, K.C. Hansen, M. Hässig, A. Jäckel, E. Kopp, A. Korth, L. Le Roy, U. Mall, R. Maggiolo, B. Marty, O. Mousis, T. Owen, H. Rème, M. Rubin, T. Sémon, C.-Y. Tzou, J.H. Waite, C. Walsh, P. Wurz, Abundant molecular oxygen in the coma of comet 67P/Churyumov-Gerasimenko, Nature 526 (2015) 678–681, https://doi.org/10.1038/nature15707.

[5] M. Rubin, K. Altwegg, H. Balsiger, A. Bar-Nun, J.-J. Berthelier, A. Bieler, P. Bochsler, C. Briois, U. Calmonte, M. Combi, J. De Keyser, F. Dhooghe, P. Eberhardt, B. Fiethe, S.A. Fuselier, S. Gasc, T.I. Gombosi, K.C. Hansen, M. Hässig, A. Jäckel, E. Kopp, A. Korth, L. Le Roy, U. Mall, B. Marty, O. Mousis, T. Owen, H. Rème, T. Sémon, C.-Y. Tzou, H. Waite, P. Wurz, Molecular nitrogen in comet 67P/Churyumov-Gerasimenko indicates a low formation temperature, Science 348 (6231) (2015) 232–235, https://doi.org/10.1126/science.aaa6100.

[6] F. Dhooghe, J. De Keyser, K. Altwegg, C. Briois, H. Balsiger, J.-J. Berthelier, U. Calmonte, G. Cessateur, M.R. Combi, E. Equeter, B. Fiethe, N. Fray, S. Fuselier, S. Gasc, A. Gibbons, T. Gombosi, H. Gunell, M. Hässig, M. Hilchenbach, L. Le Roy, R. Maggiolo, U. Mall, B. Marty, E. Neefs, H. Rème, M. Rubin, T. Sémon, C.-Y. Tzou, P. Wurz, Halogens as tracers of protosolar nebula material in comet 67P/Churyumov-Gerasimenko, MNRAS 472 (2017) 13361345, https://doi.org/10.1093/mnras/stx1911.

[7] J.-J. Berthelier, J.-M. Illiano, D. Nevejans, E. Neefs, E. Arijs, N. Schoon, High resolution focal plane detector for a space-borne magnetic mass spectrometer, Int. J. Mass Spectrom. 215 (1–3) (2002) 89–100, https://doi.org/10.1016/S1387-3806(02)00527-4.

[8] D. Nevejans, E. Neefs, S. Kavadias, P. Merken, C. Van Hoof, The LEDA512 integrated circuit anode array for the analog recording of mass spectra, Int. J. Mass Spectrom. 215 (1) (2002) 77–87, https://doi.org/10.1016/S1387-3806(01)00549-8.

[9] C.-Y. Tzou, Calibrations of ROSINA-COPS and Observations at Comet 67P/Churyumov-Gerasimenko, Ph.D. thesis, Physikalisches Institut, Universität Bern, Switzerland, 2017.

[10] E. Neefs, J.-M. Illiano, D. Nevejans, DFMS MCP-LEDA Detector Calibration in CASYMS – Flight Spare Model, Tech. Rep. ROS-BIRA-RP-15, Belgian Institute for Space Aeronomy, 2002.

[11] P. Eberhardt, K. Altwegg, DFMS Instrument Modes and Measurement Sequences, Appendix D1 to the ROSINA User Manual, Tech. Rep. RO-ROS-MAN-1010, Universität Bern, 2002.

[12] L. Giudicotti, Time dependent model of gain saturation in microchannel plates and channel electron multipliers, Nucl. Instrum. Methods A 659 (2011) 336–347, https://doi.org/10.1016/j.nima.2011.07.017.

[13] F.F. Umarov, A.A. Dzhurakhalov, Ion bombardment-induced surface effects in materials, IntechOpen (2016) 359–391, https://doi.org/10.5772/62731. Ch. 14.

[14] P.M.L. Hedberg, P. Peres, F. F, L. Renaud, Multiple ion counting measurement strategies by SIMS – a case study from nuclear safeguards and forensics, J. Anal. At. Spectrom. 30 (2015) 2516–2524, https://doi.org/10.1039/c5ja00382b.

[15] I. Schroeder, K. Altwegg, H. Balsiger, J.-J. Berthelier, J. De Keyser, B. Fiethe, S.A. Fuselier, S. Gasc, T.I. Gombosi, M. Rubin, T. Sémon, C.-Y. Tzou, S.F. Wampfler, P. Wurz, $^{16}O/^{18}O$ ratio in water in the coma of comet 67P/Churyumov-Gerasimenko measured with the Rosetta/ROSINA double-focusing mass spectrometer, A&A 33806 (2018) 1–12, https://doi.org/10.1051/0004-6361/201833806.

[16] J. De Keyser, K. Altwegg, A. Gibbons, F. Dhooghe, H. Balsiger, J.-J. Berthelier, S.A. Fuselier, T.I. Gombosi, E. Neefs, M. Rubin, Position-dependent microchannel plate gain correction in Rosetta's ROSINA/DFMS mass spectrometer, Int. J. Mass Spectrom. 446 (2019) 116232, https://doi.org/10.1016/j.ijms.2019.116232.

[17] H.O. Funsten, R.W. Harper, E.E. Dors, P.A. Janzen, B.A. Larsen, E.A. MacDonald, D.I. Poston, S.M. Ritzau, R.M. Skoug, T.H. Zurbuchen, Comparative response of microchannel plate and channel electron multiplier detectors to penetrating radiation in space, IEEE Trans. Nucl. Sci. 62 (5) (2015) 2283–2293, https://doi.org/10.1109/TNS.2015.2464174.

[18] A.S. Tremsin, O.H.W. Siegmund, Charge cloud asymmetry in detectors with biased mcps, in: Proceedings of SPIE vol. 4497, The International Society for Optical Engineering, 2001, https://doi.org/10.1117/12.454218.

[19] L. Le Roy, K. Altwegg, H. Balsiger, J.-J. Berthelier, A. Bieler, C. Briois, U. Calmonte, M.R. Combi, J. De Keyser, F. Dhooghe, B. Fiethe, S.A. Fuselier, S. Gasc, T.I. Gombosi, M. Hässig, A. Jäckel, M. Rubin, C.-Y. Tzou, Inventory of the volatiles on comet 67P/Churyumov-Gerasimenko from Rosetta/ROSINA, A&A 583 (26450) (2015) A1, https://doi.org/10.1051/0004-6361/201526450.

[20] K. Altwegg, H. Balsiger, J.-J. Berthelier, A. Bieler, U. Calmonte, S.A. Fuselier, F. Goesmann, S. Gasc, T.I. Gombosi, L. Le Roy, J. De Keyser, A. Morse, M. Rubin, M. Schuhmann, M.G.G.T. Taylor, C.-Y. Tzou, I. Wright, Organics in 67P - a first comparative analysis of mass spectra from ROSINA-DFMS, COSAC and Ptolemy, MNRAS 469 (2017) S130–S141, https://doi.org/10.1093/mnras/stx1415.

[21] M. Hässig, Sensitivity and Fragmentation Calibration of the ROSINA Double Focusing Mass Spectrometer, Ph.D. thesis, Universität Bern, 2013.

[22] National Institute of Standards and Technology, NIST chemistry WebBook. https://webbook.nist.gov/chemistry, 2019.

[23] E.R. Cawthron, Secondary electron emission from solid surfaces bombarded by medium energy ions, Aust. J. Phys. 24 (1971) 859–869, https://doi.org/10.1071/PH710859.

[24] R.J. Beuhler, L. Friedman, A model of secondary electron yields from atomic and polyatomic ion impacts on copper and tungsten surfaces based upon stopping-power calculations, J. Appl. Phys. 48 (9) (1977) 3928–3936, https://doi.org/10.1063/1.324267.

[25] J. Ferron, E.V. Alonso, R.A. Baragiola, A. Oliva-Florio, Electron emission from molybdenum under ion bombardment, J. Phys. D Appl. Phys. 14 (1981) 1707–1720, https://doi.org/10.1088/0022-3727/14/9/018.

[26] C. Lemell, J. Stöckl, J. Burgdörfer, G. Betz, H. Winter, F. Aumayr, Separation of potential and kinetic electron emission in HCl surface interactions, Phys. Scr. T80 (1998) 76–78, https://doi.org/10.1238/Physica.Topical.080a00076.

[27] Y.-Y. Wang, Y.-T. Z, J.-R. S, D.-H. Li, A. Qayyum, J.-Y. Li, P.-Z. Wang, G.-Q. Xiao, Potential and kinetic electron emissions from Hopg surface irradiated by highly charged xenon and neon ions, Chin. Phys. Lett. 28 (5) (2011), 053402, https://doi.org/10.1088/0256-307X/28/5/053402.

[28] R.A. Baragiola, Current topics in kinetic electron emission from solids, in: A. Gras-Marti, H.M. Urbassek, N.R. Arista, F. Flores (Eds.), Interaction of Charged Particles with Solids and Surfaces, vol. 271, Springer, Boston, MA, 1991, pp. 443–458, https://doi.org/10.1007/978-1-4684-8026-9_19, of Nato ASI Series (Series B: Physics).

[29] J. Lörinčík, Z. Šroubek, H. Eder, F. Aumayr, H. Winter, Kinetic electron emission from clean polycrystalline gold induced by impact of slow C^+, N^+, O^+, Ne^+, Xe^+, and Au^+ ions, Phys. Rev. B 62 (23) (2000) 16116–16125, https://doi.org/10.1103/PhysRevB.62.16116.

[30] H. Winter, H. Eder, F. Aumayr, J. Lörincik, Z. Sroubek, Slow-ion induced electron emission from clean metal surfaces: "Subthreshold kinetic emission" and "potential excitation of plasmons", Nucl. Instrum. Methods B 182 (1–4) (2001) 15–22, https://doi.org/10.1016/S0168-583X(01)00649-8.

[31] R. Meier, P. Eberhardt, Velocity and ion species dependence of the gain of microchannel plates, Int. J. Mass Spectrom. Ion Process. 123 (1993) 19–27, https://doi.org/10.1016/0168-1176(93)87050-3.

[32] B. Brehm, J. Grosser, T. Ruscheinski, M. Zimmer, Absolute detection efficiencies of a microchannel plate detector for ions, Meas. Sci. Technol. 6 (1995) 953–958, https://doi.org/10.1088/0957-0233/6/7/015.

[33] J. Oberheide, P. Wilhelms, M. Zimmer, New results on the absolute ion detection efficiencies of a microchannel plate, Meas. Sci. Technol. 8 (1997) 351–354, https://doi.org/10.1088/0957-0233/8/4/001.

[34] B. Schläppi, Characterization of the ROSINA Double Focusing Mass Spectrometer, Ph.D. thesis, Universität Bern, 2011.

[35] S. Graf, K. Altwegg, H. Balsiger, A. Jäckel, E. Kopp, U. Langer, W. Luithardt,

C. Westermann, P. Wurz, A cometary neutral gas simulator for gas dynamic sensor and mass spectrometer calibration, J. Geophys. Res. 109 (7) (2004) 1–13, https://doi.org/10.1029/2003JE002188.
[36] J. De Keyser, F. Dhooghe, A. Gibbons, K. Altwegg, H. Balsiger, J.-J. Berthelier, C. Briois, U. Calmonte, G. Cessateur, E. Equeter, B. Fiethe, S.A. Fuselier, T.I. Gombosi, H. Gunell, M. Hässig, L. Le Roy, R. Maggiolo, E. Neefs, M. Rubin, T. Sémon, Correcting peak deformation in Rosetta's ROSINA/DFMS mass spectrometer, Int. J. Mass Spectrom. 393 (2015) 41–51, https://doi.org/10.1016/j.ijms.2015.10.010.
[37] J.L. Wiza, Microchannel plate detectors, Nucl. Instrum. Methods 162 (1979) 587–601.
[38] J.G. Timothy, Review of multianode microchannel array detector systems, J. Astronomical Telesc. Instrum. Syst. 2 (3) (2016), 030901, https://doi.org/10.1117/1.JATIS.2.3.030901.
[39] E.H. Eberhardt, Gain model for microchannel plates, Appl. Opt. 18 (9) (1979) 1418–1423, https://doi.org/10.1364/AO.18.001418.
[40] H. Kume, K. Koyama, K. Nakatsugawa, S. Suzuki, D. Fatlowitz, Ultrafast microchannel plate photomultipliers, Appl. Opt. 27 (6) (1988) 1170–1178, https://doi.org/10.1364/AO.27.001170.
[41] D.C. Slater, T.J. Gethyn, Microchannel plate modal gain variations with temperature, Rev. Sci. Instrum. 64 (2) (1993) 430–435, https://doi.org/10.1063/1.1144212.